Front. Mech. Eng. 2020, 15(4): 547–557
https://doi.org/10.1007/s11465-020-0595-1

RESEARCH ARTICLE

Xiaojun GU, Xiuzhong SU, Jun WANG, Yingjie XU, Jihong ZHU, Weihong ZHANG

Improvement of impact resistance of plain-woven composite by embedding superelastic shape memory alloy wires

Abstract Carbon fiber reinforced polymer (CFRP) composites have excellent mechanical properties, specifically, high specific stiffness and strength. However, most CFRP composites exhibit poor impact resistance. To overcome this limitation, this study presents a new plain-woven CFRP composite embedded with superelastic shape memory alloy (SMA) wires. Composite specimens are fabricated using the vacuum-assisted resin injection method. Drop-weight impact tests are conducted on composite specimens with and without SMA wires to evaluate the improvement of impact resistance. The material models of the CFRP composite and superelastic SMA wire are introduced and implemented into a finite element (FE) software by the explicit user-defined material subroutine. FE simulations of the drop-weight impact tests are performed to reveal the superelastic deformation and debonding failure of the SMA inserts. Improvement of the energy absorption capacity and toughness of the SMA-CFRP composite is confirmed by the comparison results.

Keywords carbon fiber reinforced polymer composite, shape memory alloy wire, impact resistance, drop-weight test, finite element simulation

Received January 8, 2020; accepted March 20, 2020

Xiaojun GU, Jun WANG (✉)
Unmanned System Research Institute, Northwestern Polytechnical University, Xi'an 710072, China
E-mail: wang.jun@nwpu.edu.cn

Xiaojun GU, Xiuzhong SU, Jun WANG, Yingjie XU (✉), Jihong ZHU, Weihong ZHANG
State IJR Center of Aerospace Design and Additive Manufacturing, Northwestern Polytechnical University, Xi'an 710072, China
E-mail: xu.yingjie@nwpu.edu.cn

Yingjie XU, Jihong ZHU
Shaanxi Engineering Laboratory of Aerospace Structure Design and Application, Northwestern Polytechnical University, Xi'an 710072, China

1 Introduction

Carbon fiber reinforced polymer (CFRP) is an extremely strong and lightweight composite material. Owing to its high specific mechanical properties, CFRP is used in a wide variety of engineering applications, such as in aerospace, automotive, electromechanical, and biomedical fields. However, most CFRP composites exhibit poor impact resistance, mainly because the localized impact loading leads easily to delamination within the thickness of the composite and debonding in the interface between the fiber and matrix. In engineering practice, improving the impact resistance of CFRP composites remains a challenging issue. In recent years, an increasing number of researchers [1–3] have paid attention to this topic. For example, Cantwell and Morton [4], Richardson and Wisheart [5], and Agrawal et al. [6] summarized related studies on the impact behavior of fiber-reinforced composites.

Over the last decades, substantial effort was exerted to reveal the impact behavior and fracture mechanism of CFRP composites. Meanwhile, various approaches were proposed to improve the impact resistance, damping capacity, and toughness of CFRP composites. Sayer et al. [7] experimentally investigated the impact behavior of hybrid composite plates and used the energy profiling method to determine the penetration and perforation thresholds of the composites. The experimental results showed that the perforation threshold of carbon fibers is 30% higher than that of glass fibers. Yang and Cantwell [8] conducted low velocity impact tests on a glass fiber-reinforced epoxy resin to investigate the effect of impact parameters, including test temperature, target size, and impactor geometry, on the damage initiation threshold. Polimeno et al. [9] studied the low-velocity impact damage and nonlinear material response of CFRP composites and employed the nonlinear image technique to evaluate the defect position. Wang et al. [10] investigated the low-velocity impact characteristics and residual tensile strength of CFRP composite lattice core sandwiched structures and

divided the degradation of residual tensile strength into three stages for different impact energies. Meanwhile, Batra et al. [11] and Shi et al. [12] examined the damage initiation, growth, cracking, and fracture mechanisms of CFRP composites under low-velocity impact loading. Quaresimin et al. [13] investigated the impact behavior of CFRP composite laminates under low-velocity impact and considered the influence of stacking sequence and laminate thickness. In addition, the authors introduced a new approach for assessing the energy absorption capacity of the CFRP composite laminates. Long et al. [14] presented a damage analysis process for composite laminates subjected to low-velocity impact, and the delamination area was found to be distributed symmetrically around the impact point. These studies revealed several basic deformation and fracture mechanisms of CFRP composites. In general, impact damage in CFRP composites involves three processes, that is, damage initiation at the defect and crack growth in the matrix, delamination between the matrix and fibers, and the fracture of fibers. Traditional methods for improving impact resistance involve eliminating defects and strengthening matrices and fibers. However, impact resistance improvement is relatively limited if no creative methodology is introduced.

Shape memory alloy (SMA) is a typical smart material that features the shape memory effect and superelasticity. Owing to stress-induced martensitic phase transformation that occurs at the crystalline scale, SMAs exhibit large reversible transformation strain and hysteretic dissipation. The high damping capacity and sufficient mechanical properties of SMAs make them one of the most promising materials for energy absorption, especially against impact loading. The combination of SMAs with CFRP composites provides new opportunities for improving the impact resistance and toughness of the composites. Several researchers conducted related works. For example, Jung et al. [15] fabricated an air intake structure using an SMA-embedded composite that can generate a comparatively large actuating force by applying an electric current through the embedded SMA wires. Raghavan et al. [16] designed an SMA fiber-reinforced composite to enhance the damping capacity and toughness of a polymer matrix, and appreciable improvement was observed in the damping, tensile, and impact properties of the composite. Wierschem and Andrawes [17] studied an SMA-FRP composite for potential use in concrete structures, and the results showed that the SMA-FRP composite could improve the ductile and damping of the concrete structures and maintain their elastic characteristic. Panda and Singh [18] numerically investigated the nonlinear free vibration behavior of an SMA-embedded composite panel, and the results indicated that nonlinear frequency parameters can be suppressed by adding SMA fibers to a parent composite without an external controller. Rodrigue et al. [19] designed a smart soft composite actuator by combining four SMA wires in a soft matrix, and the actuator exhibited multiple actuation modes, including bending and twisting. Daghash and Ozbulut [20] investigated the cyclic behavior of an SMA-FRP composite, and the results revealed that the SMA-FRP composite can recover from relatively high strain upon unloading and exhibit very high failure strain. Sofocleous et al. [21] compared the energy absorption and damage development of a CFRP composite reinforced with an SMA wire and a carbon nanotube, and the SMA-reinforced CFRP composite exhibited high energy absorption. When the two components were combined, though the energy absorption improvement of the carbon nanotube-reinforced CFRP composite is the same as that of the SMA-reinforced CFRP composite, toughness is increased by the addition of the carbon nanotube. El-Tahan and Dawood [22] studied the bond behavior of NiTiNb SMA wires embedded in CFRP composites, and the results indicated that interfacial bond transfer consists of two components, that is, cohesion before the onset of debonding and friction after the onset of debonding. Mahmood Baitab et al. [23] reviewed techniques for embedding SMA wires in smart woven composites, and the SMA-embedded smart composites demonstrated tunable properties, active abilities, damping capacity, and self-healing properties. Quade et al. [24] studied the effect of thin film adhesives on mode II interlaminar fracture toughness in carbon fiber composites with SMA inserts, and the addition of the SMA material between plies exacerbates this failure mode. Eslami-Farsani et al. [25,26] studied the effects of SMA wires on the buckling and impact responses of fiber metal laminates, and the results showed that the embedding of SMA wires enhances buckling and impact resistance. Moreover, the enhancing effect is sensitive to the SMA volume fraction and applied prestrain. Meanwhile, Pazhanivel et al. [27,28] examined the impact resistance of glass fiber reinforced polymer (GFRP) composite laminates reinforced with randomly oriented short strips of SMA under different temperatures and observed that the SMA-GFRP composite laminates exhibit enhanced damage resistance at high temperatures, whereas the addition of the SMA reinforcement contributes little in such a case.

The above literature review well demonstrates the improvement of the impact resistance of CFRP composites embedded with SMA wires or thin films. However, the localized phase transformation of SMA inserts, the deformation and fracture modes of a CFRP matrix, and the debonding behavior between SMA inserts and CFRP composites are not well understood. Thus, we initiated this work to address the above issues. Low-velocity impact tests with different impact energies were conducted on SMA-embedded CFRP composites, and finite element (FE) simulation was conducted to further examine impact and fracture mechanisms.

This paper is organized as follows. Section 2 presents the experiments on the SMA-CFRP composite specimens, and Section 3 introduces the material models of the

superelastic SMA wire and CFRP composite. Section 4 details the FE simulation of the SMA-CFRP composite specimens against impact, and Section 5 discusses the simulation results and compares them with those of the experiments. Finally, Section 6 draws conclusions from the present study.

2 Experiments

2.1 Materials

SMA-embedded CFRP composites mainly comprise the plain-woven carbon fabrics, the epoxy resin, and the superelastic SMA wires. The T300 plain-woven carbon fabrics are supplied by TORAY Composite Co., Ltd., Japan, and the Young's modulus and Poisson's ratio of the carbon fiber are 220 GPa and 0.26, respectively. The thickness of each fabric layer is 0.2 mm, and the specific density is 200 g/m^2. The matrix materials are supplied by Shanghai AXSON Co., Ltd., China, including the EPOLAM 5015 epoxy resin and the RSF816 hardening agent, and the mass proportion of both is 100:36. The Young's modulus of the solid epoxy resin is 2 GPa, and the Poisson's ratio is 0.4. The SMA wires used in the present study are NiTi alloy with a composition of 50.8 at.% Ni and manufactured by Xi'an Saite Metal Materials Co., Ltd., China. The diameter of the SMA wire is 0.5 mm. The transformation temperatures of the SMA wires are measured by a NETZSCH DSC 200F3 machine, which are the martensite finish temperature ($M_f = -110$ °C), the martensite start temperature ($M_s = -70$ °C), the austenite start temperature ($A_s = -31$ °C), and the austenite finish temperature ($A_f = -15$ °C). The relatively low austenite finish temperature (A_f) can guarantee the SMA wires in the austenite phase and that they exhibit complete superelasticity at room temperature.

2.2 Fabrication of SMA-CFRP composite specimens

The SMA-CFRP composite specimens are fabricated using the vacuum-assisted resin injection (VARI) method. The laminate specimen comprises four layers of plain-woven carbon fabric, and the SMA wires are placed parallel between the bottom two layers. The SMA wires are well polished to improve interfacial bounding with the epoxy resin. Figure 1 presents the composition diagram and fabricated SMA-CFRP composite specimen. The specimens are cut into 150 mm × 150 mm squares using a water jet cutting machine. The fabrication process is detailed in Ref. [29]. To demonstrate the improvement of the impact resistance of SMA-CFRP composites, CFRP composite specimens without embedded SMA wires are also fabricated using the same fabrication process and geometry.

2.3 Drop-weight impact tests

Drop-weight impact tests are conducted on the Instron CEAST 9340 impact machine, and the photograph and schematic representation of the impact machine are shown in Fig. 2. The machine consists mainly of three components, namely, the drop hammer device, the clamping fixture, and the data acquisition system. The mass and diameter of the steel drop hammer are 3.74 kg and 20 mm, respectively. The impact tests are performed at room temperature, and two impact energies of 10 and 30 J are considered. The specimens are bolted between the fixture and clamp bars to prevent in-plane movement during the impact tests. As shown in Fig. 2, there is a circular hole with a diameter of 75 mm on the base fixture. During impact testing, the geometric centers of the drop hammer, the composite specimen, and the circular hole coincide with one another to guarantee the symmetry of the loading and boundary conditions. Impact forces are measured by the force sensor attached to the drop hammer. The displacement is obtained by the double integration of the force curve as

$$e_i = \iint_i \frac{F(t) - M_{\text{total}} g}{M_{\text{total}}} \mathrm{d}^2 t, \tag{1}$$

where e_i is the displacement of the impact point at time i, $F(t)$ is the impact force, M_{total} is the mass of the drop hammer, and g is the gravitational acceleration.

Figure 3 shows the deformation and damage on the SMA-CFRP and CFRP composite specimens for impact energies of 10 and 30 J. Photographs are taken from the back side of the composite specimens. Specifically, for the impact energy of 10 J, the CFRP composite specimen

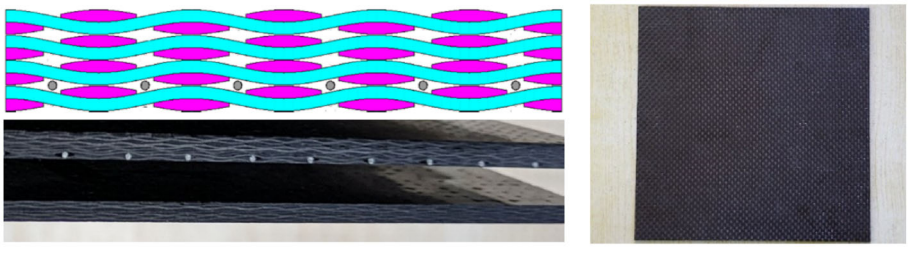

Fig. 1 SMA-embedded CFRP composite specimens.

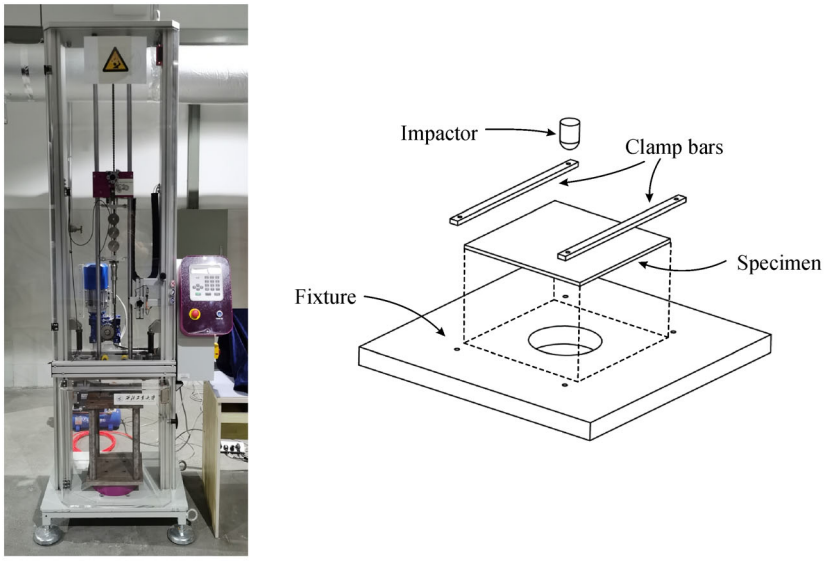

Fig. 2 Photograph and schematic representation of the drop-weight impact system.

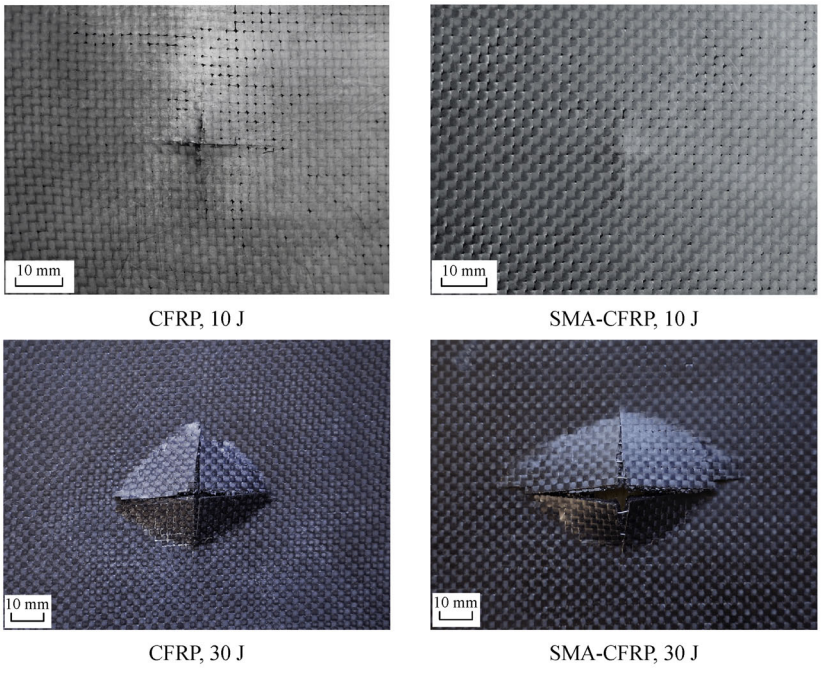

Fig. 3 Photographs of the specimens after drop-weight impact tests for impact energies of 10 and 30 J.

shows a localized cruciform crack, whereas the SMA-CFRP composite specimen does not display visible surface damage. However, a small bump deformation is observed at the impact point, thereby indicating that the damage occurred inside the composite laminate, specifically, at the resin matrix and carbon fabric. A comparison of the two photographs confirms that the embedding of superelastic SMA wires improves the impact resistance of the CFRP composite. When impact energy is increased to 30 J, the CFRP and SMA-CFRP composite specimens exhibit an obvious cruciform crack. The difference is that the two crack edges on the CFRP composite specimen are nearly equal in length owing to the in-plane isotropy of this specimen. However, this outcome is not the case with the SMA-CFRP composite specimen. The crack edge parallel to the SMA wires is long, thereby indicating that the embedding of SMA wires leads to in-plane orthotropy in the SMA-CFRP composite. In addition, the SMA-CFRP

composite specimen exhibits a large area of fracture and thus absorbs increased impact energy. This finding is presented as force and displacement curves in Section 5 and discussed in detail.

3 Material models

In this section, two material models are introduced to describe the mechanical behavior of the SMA wires and CFRP composite. The SMA model was developed by Wang et al. [30] within a thermodynamically consistent framework. The model mainly involves superelasticity, martensitic phase transformation, and the loading condition. The CFRP composite model is a generalized 3D Hashin model, including anisotropic elasticity and damage mechanisms [31], and the material parameters are obtained from the representative volume element (RVE) model comparing the resin matrix, carbon fiber, and bounding interface.

3.1 Shape memory alloy model

Superelasticity is one of the most salient material characteristics of SMA, which features complete reversible deformation and large amounts of hysteretic dissipation. Superelasticity is a consequence of stress-induced phase transformation between austenite and martensite at the temperature above the austenite finish temperature. The superelastic stress–strain relation is formulated with the following constitutive law:

$$\boldsymbol{\sigma} = p\boldsymbol{I} + \boldsymbol{s},\ p = K\delta,\ \boldsymbol{s} = 2\mu\boldsymbol{\gamma}, \tag{2}$$

where $\boldsymbol{\sigma}$ is the Cauchy stress tensor, p and $\boldsymbol{s}$ are the spherical and deviatoric components of the Cauchy stress, $\boldsymbol{I}$ is the second-order identity tensor, δ and $\boldsymbol{\gamma}$ are the spherical and deviatoric components of the logarithmic strain, and K and μ are the bulk and shear moduli, respectively.

Martensitic phase transformation refers to the first-order diffusionless phase transformation between austenite and martensite and can be induced by either applied stress or temperature change. At temperatures above the austenite finish temperature, austenite is stable at low-stress levels, whereas martensite is metastable at high stress levels. Thus, SMA transforms from austenite to martensite under applied stress (forward transformation) and recovers to the parent austenite phase when the stress is released (reverse transformation). The governing equation associated with martensitic phase transformation is

$$\dot{z} = \lambda S(\Lambda), \tag{3}$$

where $\dot{z}$ is the increment of the martensite volume fraction, λ is a nonnegative multiplier, $S(\cdot)$ is a signum function, and Λ is the thermodynamic driving force of the martensite volume fraction. Equation (3) indicates that martensite volume fraction increases when the thermodynamic driving force is positive, and vice versa. The derivation and explicit expression of Λ were detailed by Wang et al. [30]. The reversible transformation strain is linked to the martensite volume fraction as

$$\dot{\boldsymbol{\gamma}}_{\mathrm{t}} = \dot{z}h\boldsymbol{\Sigma},\ \boldsymbol{\Sigma} = \begin{cases} \dfrac{\boldsymbol{s}}{\|\boldsymbol{s}\|} & \text{if } \dot{z} \geqslant 0, \\ \boldsymbol{n} & \text{if } \dot{z} < 0, \end{cases} \tag{4}$$

where γ_{t} is the transformation strain, $\dot{\gamma}_{\mathrm{t}}$ denotes the time derivative of γ_{t}, h denotes the saturation value of the transformation strain, and $\boldsymbol{n}$ is the direction of the transformation strain. Equation (4) means that during forward transformation, the transformation strain grows in the direction of the deviatoric stress tensor, whereas the transformation strain recovers in its own direction during the reverse transformation.

The initiation, growth, and saturation of the martensitic phase transformation are determined by the loading function Eq. (5):

$$F_z = |\Lambda| - Y, \tag{5}$$

where Y is the threshold of the martensitic phase transformation. The overall phase transformation process is stated as follows:

- If the loading function $F_z \leqslant 0$, then martensitic phase transformation does not occur, and $\dot{z} = 0$.
- If the loading function $F_z > 0$ and the thermodynamic driving force $\Lambda > 0$, then forward martensitic phase transformation occurs, and $\dot{z} = \lambda$.
- If the loading function $F_z > 0$ and the thermodynamic driving force $\Lambda < 0$, then reverse martensitic phase transformation occurs, and $\dot{z} = -\lambda$.

3.2 CFRP composite model

According to the generalized 3D Hashin model, the initial elastic constants of the CFRP composite are calculated from the values of Young's modulus and Poisson's ratio as

$$\begin{cases} C^0_{xx} = E_{xx}(1 - v_{yz}v_{zy})\eta, \\ C^0_{yy} = E_{yy}(1 - v_{xz}v_{zx})\eta, \\ C^0_{zz} = E_{zz}(1 - v_{xy}v_{yx})\eta, \\ C^0_{xy} = E_{xx}(v_{yx} + v_{zx}v_{yz})\eta, \\ C^0_{yz} = E_{yy}(v_{zy} + v_{xy}v_{zx})\eta, \\ C^0_{zx} = E_{xx}(v_{zx} + v_{yx}v_{zy})\eta, \\ \eta = 1/(1 - v_{xy}v_{yx} - v_{yz}v_{zy} - v_{zx}v_{xz} - 2v_{xy}v_{yz}v_{zx}), \end{cases} \tag{6}$$

where E and v are the Young's modulus and Poisson's ratio, respectively, η is an anisotropy coefficient, and

C_*^0 (* = xx, yy, zz, xy, yz, and zx) is the elastic constants of the undamaged CFRP composite.

The generalized 3D Hashin model considers four damage mechanisms, namely, tensile fiber failure, compressive fiber failure, tensile matrix failure, and compressive matrix failure. These damage mechanisms are formulated as

$$\begin{cases} d_{\mathrm{ft}} = \left(\dfrac{\sigma_{xx}}{F_{x\mathrm{T}}}\right)^2 + \alpha\left(\dfrac{\sigma_{xy}}{F_{x\mathrm{S}}}\right)^2 + \beta\left(\dfrac{\sigma_{xz}}{F_{y\mathrm{S}}}\right)^2, & \text{if} \quad \sigma_{xx}>0, \\ d_{\mathrm{fc}} = \left(\dfrac{\sigma_{xx}}{F_{x\mathrm{C}}}\right)^2, & \text{if} \quad \sigma_{xx}<0, \\ d_{\mathrm{m}} = \left[\left(\dfrac{\sigma_{xx}}{2F_{x\mathrm{T}}}\right)^2 + \left(\dfrac{\sigma_{yy}}{|F_{y\mathrm{T}}F_{y\mathrm{C}}|}\right)^2 + \left(\dfrac{\sigma_{xy}}{F_{x\mathrm{S}}}\right)^2\right] \\ \qquad +\sigma_{yy}\left(\dfrac{1}{F_{y\mathrm{T}}}+\dfrac{1}{F_{y\mathrm{C}}}\right), \end{cases} \tag{7}$$

where d_{ft} and d_{fc} are the tensile and compressive damage factors for the fiber, d_{m} is the damage factor for the matrix, σ and F are the stress and material strength corresponding to the failure modes, and α and β are two material coefficients representing the contribution of shear stress to the failure of the fiber. The subscripts x and y represent two orthogonal material directions, and the subscripts T, C and S represent tensile, compressive and shear, respectively. These damage criteria compete with one another. Specifically, material failure occurs once any of the damage factors reach 1.

With the growth of the damage factors, the elastic constants of the CFRP composite decrease. In the damaged composite, the elastic constants in the material stiffness matrix are computed as follows:

$$\begin{cases} C_{xx} = (1-d_{\mathrm{f}})C_{xx}^0, \\ C_* = (1-d_{\mathrm{f}})(1-d_{\mathrm{m}})C_*^0, \\ G_{**} = (1-d_{\mathrm{f}})(1-s_{\mathrm{m}}d_{\mathrm{m}})^2 G_{**}^0, \\ d_{\mathrm{f}} = d_{\mathrm{ft}} + d_{\mathrm{fc}} - d_{\mathrm{ft}}d_{\mathrm{fc}}, \end{cases} \tag{8}$$

where d_{f} denotes the global damage factor for the fiber, * = yy, zz, xy, and yz, ** = xy, yz, and zx, and s_{m} is the material coefficient for controlling the loss of shear stiffness caused by matrix failure.

4 Finite element simulation

To conduct the FE simulation of the drop-weight impact tests on the SMA-CFRP and CFRP composite specimens, the material models presented in Section 3 were implemented into the FE software ABAQUS by the explicit user-defined material subroutine VUMAT.

4.1 Finite element model

Figure 4 shows the FE model of the drop-weight impact test. During the simulations, the impactor, clamp bars, and fixture were modelled using the discrete rigid body. The CFRP composite and SMA wires were meshed using eight-node reduced integration hexahedral elements (ABAQUS/Explicit C3D8R). The directions of the carbon fiber and SMA wires were in parallel. General contact was defined between the impactor, fixture, and specimen, and the contact properties included a frictionless tangential behavior and a hard contact normal behavior. To simulate the eroding behavior of the impactor into the specimen, contact was also defined between the SMA wires, the interior surfaces of the CFRP composite, and the impactor.

4.2 Cohesion model

The interfacial mechanical behavior between the SMA wires and CFRP composite was described by the cohesion model. Contact between the SMA wires and CFRP composite was modelled using cohesive surfaces. To simulate the debonding behavior between the SMA wires and CFRP composite, the quadratic separation criterion was used as the damage initiation criterion, and the damage evolution criterion is a power law given by

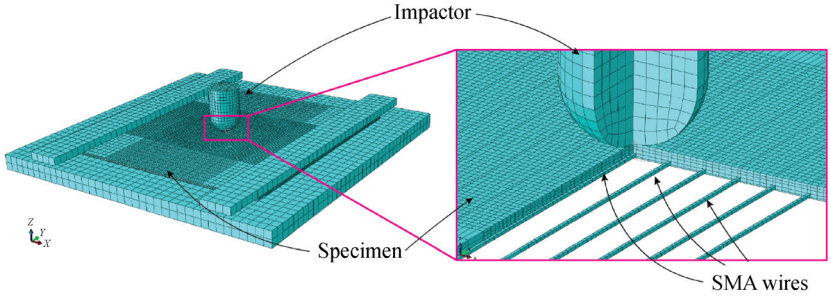

Fig. 4 Finite element model of drop-weight impact test.

$$\begin{cases} \left(\dfrac{\langle\delta_{\mathrm{n}}\rangle}{\delta_{\mathrm{n}}^{\max}}\right)^2+\left(\dfrac{\delta_{\mathrm{s}}}{\delta_{\mathrm{s}}^{\max}}\right)^2+\left(\dfrac{\delta_{\mathrm{t}}}{\delta_{\mathrm{t}}^{\max}}\right)^2=1, \\ \qquad \text{damage initiation}, \\ \left(\dfrac{G_{\mathrm{n}}}{G_{\mathrm{n}}^{\mathrm{C}}}\right)^{\alpha}+\left(\dfrac{G_{\mathrm{s}}}{G_{\mathrm{s}}^{\mathrm{C}}}\right)^{\alpha}+\left(\dfrac{G_{\mathrm{t}}}{G_{\mathrm{t}}^{\mathrm{C}}}\right)^{\alpha}=1, \\ \qquad \text{damage evolution}, \end{cases} \tag{9}$$

where $\langle\ \rangle$ represents the Macaulay bracket signifying that a purely compressive displacement or stress state did not initiate the damage, δ and $\delta^{\max}$ represent the contact separation and the corresponding peak value, G represent the work done by the traction and their conjugate separation, and G^{C} represent the critical fracture energy required to initiate failure. The subscript "n" represents the normal direction, and the subscripts "s" and "t" represent two shear directions. These model parameters are listed in Table 1 and obtained from Yang et al. [32].

5 Results and discussions

In this section, the simulation results are discussed and compared with the experimental results. First, the deformations and failures of the SMA-CFRP and CFRP composite specimens for impact energies of 10 and 30 J are compared. Next, the simulated failure profiles are compared with the experimental photographs for the impact energy of 30 J. Finally, the impact force and displacement curves are plotted to further reveal the mechanical behavior of the SMA-CFRP and CFRP composite specimens under impact loadings.

Figure 5 presents the simulated postimpact deformation and damage on the CFRP and SMA-CFRP composite specimens for impact energies of 10 and 30 J. To highlight the deformation and damage on the composite specimens, the impactor and fixture shown in Fig. 4 are not presented. In the CFRP composite specimens (two figures on the left in Fig. 5), a localized cruciform crack occurs at the impact point, which grows as the impact energy increases. Meanwhile, delamination damage is observed, which is

Table 1 Parameters of cohesion-based damage criterion obtained from Yang et al. [32]

Unit volume force/($\mathrm{N\cdot m^{-3}}$)			Separation distance/(10^{-6} mm)			Unit length force/($\mathrm{N\cdot m^{-1}}$)		
K_{n}	K_{s}	K_{t}	$\delta_{\mathrm{n}}^{\max}$	$\delta_{\mathrm{s}}^{\max}$	$\delta_{\mathrm{t}}^{\max}$	$G_{\mathrm{n}}^{\mathrm{C}}$	$G_{\mathrm{s}}^{\mathrm{C}}$	$G_{\mathrm{t}}^{\mathrm{C}}$
500	310	310	1.5	11	11	0.42	0.42	0.42

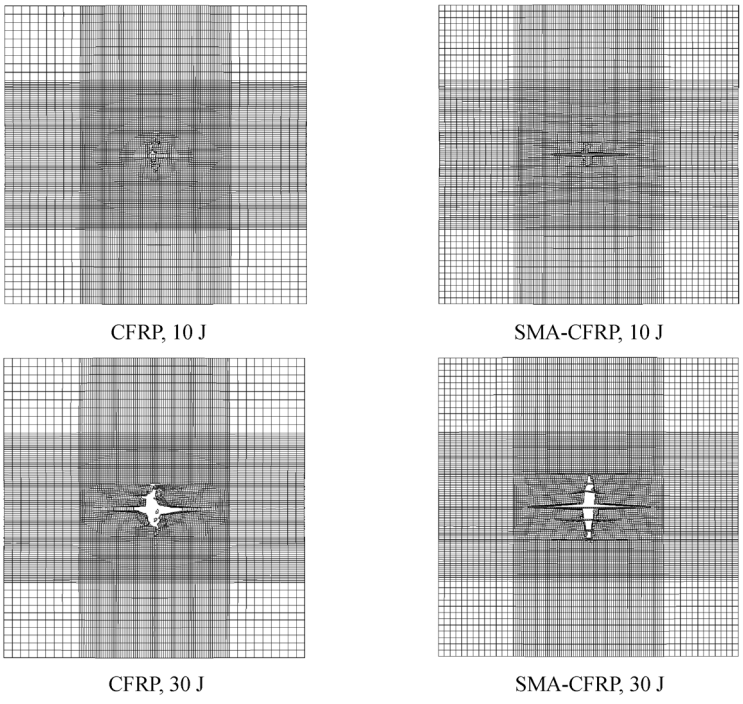

Fig. 5 Simulation results of drop-weight impact tests for impact energies of 10 and 30 J.

barely detected in the experimental observation but clearly highlighted in the FE simulation. However, the SMA-CFRP composite specimens exhibit main cracks parallel to the SMA wires. Moreover, in the impact test of the SMA-CFRP composite for the impact energy of 10 J, the specimen does not show visible surface damage, but the simulated results indicate a crack along the SMA wires next to the impact point. In fact, this crack results from debonding between the SMA wires and matrix, which occurred in the experiments inside the composite. However, this damage phenomenon is concealed by the soft epoxy resin layer on the surface. In the simulation, a cohesion-based damage criterion is used to simulate the debonding behavior of the SMA wires, which leads to a strong stress concentration at the bottom fabric layer and thus surface damage. At the impact energy of 30 J, the SMA-CFRP composite specimen exhibits multiple cracks along the SMA wires, which coincides with the in-plane orthotropic damage behavior observed in the experiment. This anisotropic damage occurs only in CFRP composites reinforced with continuous SMA fibers. Pazhanivel et al. [27] studied the impact damage resistance of GFRP composites reinforced with randomly oriented short SMA fibers, and the experimental images showed that the damage behavior is approximately isotropic.

To provide a visible comparison between the simulated results and the experimental photographs, Fig. 6 shows the side view of the deformation and damage on the CFRP and SMA-CFRP composite specimens for the impact energy of 30 J. Overall, based on the comparison of Figs. 3, 5, and 6, the simulated results reasonably duplicate the experimental findings, that is, improvement of the impact resistance and in-plane orthotropy of a CFRP composite by embedding SMA wires. The improvement of impact resistance is attributable to the following two factors: (i) The embedding of SMA wires promotes mechanical properties, specifically, the elastic modulus of the entire composite, and (ii) SMA wires exhibit superelasticity, which can dissipate large amounts of impact energy. In other words, stiffness, strength, and damping capacity are increased when SMA wires are embedded appropriately in the CFRP composite. However, if the volume fraction of the SMA wires exceeds a certain value, then the mechanical properties and impact resistance are expected to degrade owing to discontinuity [25].

Figure 7 shows the evolution of the impact forces of the SMA-CFRP and CFRP composite specimens for impact energies of 10 and 30 J. The solid curves represent the experimental (EXP) data, and the dashed curves represent the simulation (SIM) results. The time duration of the impact process for 10 J is 10 ms, and that for 30 J is within 8 ms. The peak force represents the load-bearing capacity of the composite specimens. In the first half of the impact process, impact forces increase rapidly and achieve maximum values at approximately 2 ms. The fluctuations on the curves are mainly because of the stress wave effect during the propagation of the contact force inside the composite specimens. In the second half, impact forces return to zero as the drop hammer detaches from the specimens.

Figure 8 shows the force-displacement curves of the CFRP and SMA-CFRP composite specimens for impact energies of 10 and 30 J. For the impact energy of 10 J, the curves display hysteresis loops, and the size of the loops implies the amount of the dissipated energy under impact loading. For the impact energy of 30 J, the SMA-CFRP composite dissipates more energy than the CFRP composite. The increasing displacement means that the impactor penetrates the composite specimens. Overall, the simulated results have satisfactory correlation with the experimental

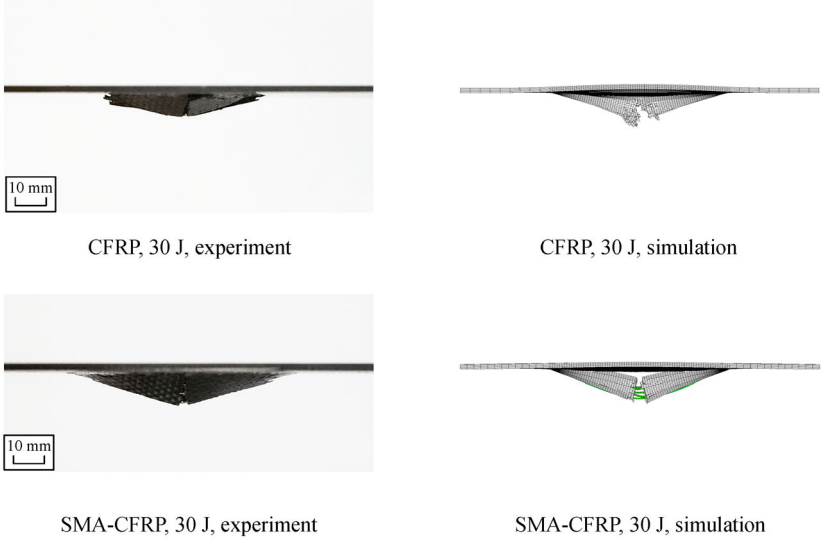

Fig. 6 Comparisons between experimental photographs and simulation results: Deformation and damage on the CFRP and SMA-CFRP composite specimens for the impact energy of 30 J.

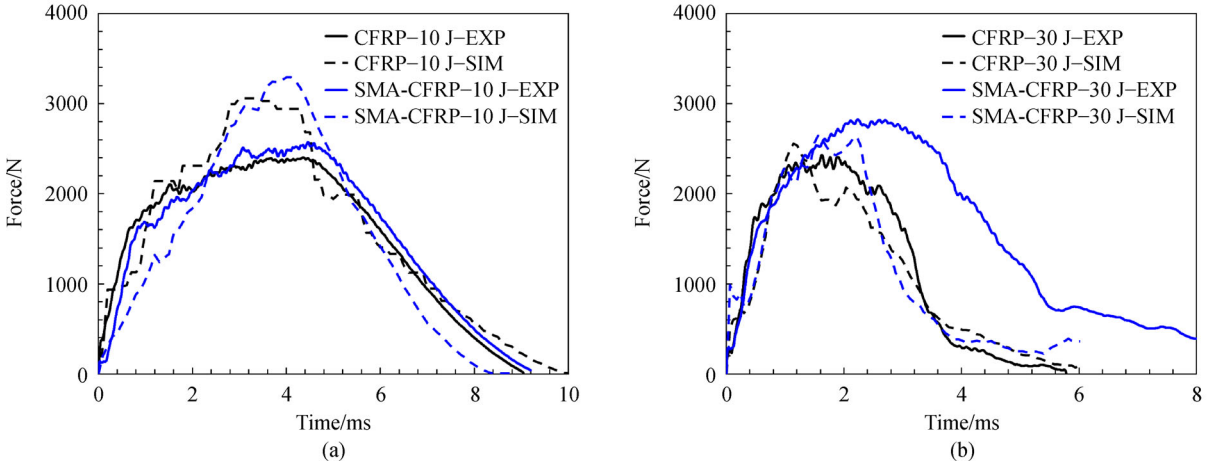

Fig. 7 Impact forces of CFRP and SMA-CFRP composite specimens for impact energies of (a) 10 and (b) 30 J. EXP: Experimental; SIM: Simulation.

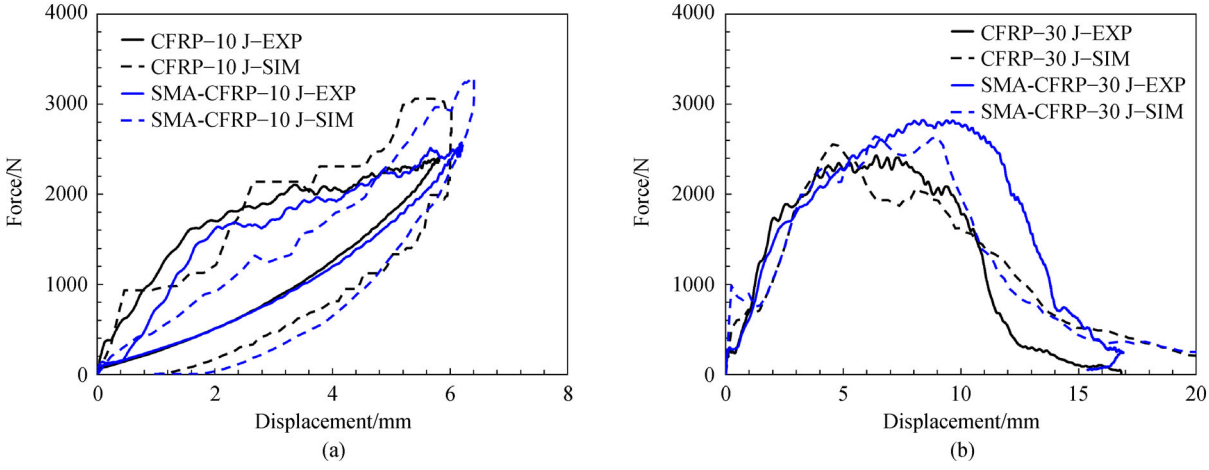

Fig. 8 Impact force–displacement curves of CFRP and SMA-CFRP composite specimens for impact energies of (a) 10 and (b) 30 J. EXP: Experimental; SIM: Simulation.

data, and the maximum deviation occurs in the SMA-CFRP composite for the impact energy of 30 J. This finding is mainly because, in practice, the debonding behavior between the SMA wires and composite matrix demonstrates high complexity and nonlinearity. In the present simulations, for numerical conciseness, a quadratic separation criterion is used to approximate the failure of the cohesive surface. Thus, large-scale debonding behavior at a strong impact energy of 30 J contributes to the differences between the simulated results and experimental data, which may be addressed by introducing a highly sophisticated damage criterion for cohesive surfaces.

6 Conclusions

In this study, the impact resistance of SMA-CFRP and CFRP composite specimens was compared through experimental and numerical methods, and the results well demonstrated the improved impact resistance of the SMA-CFRP composite. The SMA-CFRP composite specimens were fabricated using the VARI method, with four layers of plain-woven carbon fabric and SMA wires embedded parallel between the bottom two carbon fabric layers. The drop-weight impact tests of the SMA-CFRP and CFRP composite specimens were conducted on the Instron CEAST 9340 impact machine. At the impact energy of 10 J, the CFRP composite specimen showed a cruciform crack, whereas the SMA-CFRP composite specimen exhibited only a small bump deformation, which confirmed improved impact resistance. When the impact energy was increased to 30 J, both specimens exhibited a visible cruciform crack. The long crack edge along the SMA wires indicated that the embedding of SMA wires led to a high energy absorption capability and in-plane orthotropy in SMA-CFRP composites.

The material models of the SMA wire and CFRP composite were introduced for the FE simulation of the impact tests. The simulation results indicated satisfactory correlation with the experimental phenomena, and the crack morphology and force–displacement response were duplicated with a high degree of similarity. Stiffness, strength, and damping capacity were enhanced by embedding SMA wires in the CFRP composite. Consequently, the SMA-CFRP composite showed improved load bearing and energy absorption capacities. Debonding between the SMA wires and CFRP composite was the major factor resulting in impact damage on the SMA-CFRP composites. To further improve the impact resistance of the SMA-CFRP composite, new specimens will be fabricated with orthogonally embedded SMA wires and sandwiched 2D SMA thin film lattices in the near future, which are expected to address debonding risks.

Acknowledgements This work was supported by the National Natural Science Foundation of China (Grant Nos. 11802243 and 11802241).

References

1. Yoshimura A, Nakao T, Yashiro S, et al. Improvement on out-of-plane impact resistance of CFRP laminates due to through-the-thickness stitching. Composites. Part A, Applied Science and Manufacturing, 2008, 39(9): 1370–1379
2. Takagaki N, Okubo K, Fujii T. Improvement of fatigue strength and impact properties of plain-woven CFRP modified with micro fibrillated cellulose. Advanced Materials Research, 2008, 47–50: 133–136
3. Blok L G, Kratz J, Lukaszewicz D, et al. Improvement of the in-plane crushing response of CFRP sandwich panels by through-thickness reinforcements. Composite Structures, 2017, 161: 15–22
4. Cantwell W J, Morton J. The impact resistance of composite materials—A review. Composites, 1991, 22(5): 347–362
5. Richardson M O W, Wisheart M J. Review of low-velocity impact properties of composite materials. Composites. Part A, Applied Science and Manufacturing, 1996, 27(12): 1123–1131
6. Agrawal S, Singh K K, Sarkar P K. Impact damage on fibre-reinforced polymer matrix composite—A review. Journal of Composite Materials, 2014, 48(3): 317–332
7. Sayer M, Bektaş N B, Sayman O. An experimental investigation on the impact behavior of hybrid composite plates. Composite Structures, 2010, 92(5): 1256–1262
8. Yang F J, Cantwell W J. Impact damage initiation in composite materials. Composites Science and Technology, 2010, 70(2): 336–342
9. Polimeno U, Meo M, Almond D P, et al. Detecting low velocity impact damage in composite plate using nonlinear acoustic/ultrasound methods. Applied Composite Materials, 2010, 17(5): 481–488
10. Wang B, Wu L Z, Ma L, et al. Low-velocity impact characteristics and residual tensile strength of carbon fiber composite lattice core sandwich structures. Composites. Part B, Engineering, 2011, 42(4): 891–897
11. Batra R C, Gopinath G, Zheng J Q. Damage and failure in low energy impact of fiber-reinforced polymeric composite laminates. Composite Structures, 2012, 94(2): 540–547
12. Shi Y, Swait T, Soutis C. Modelling damage evolution in composite laminates subjected to low velocity impact. Composite Structures, 2012, 94(9): 2902–2913
13. Quaresimin M, Ricotta M, Martello L, et al. Energy absorption in composite laminates under impact loading. Composites. Part B, Engineering, 2013, 44(1): 133–140
14. Long S, Yao X, Zhang X. Delamination prediction in composite laminates under low-velocity impact. Composite Structures, 2015, 132: 290–298
15. Jung B S, Kim M S, Kim J S, et al. Fabrication of a smart air intake structure using shape memory alloy wire embedded composite. Physica Scripta, 2010, 2010(T139): 014042
16. Raghavan J, Bartkiewicz T, Boyko S, et al. Damping, tensile, and impact properties of superelastic shape memory alloy (SMA) fiber-reinforced polymer composites. Composites. Part B, Engineering, 2010, 41(3): 214–222
17. Wierschem N, Andrawes B. Superelastic SMA–FRP composite reinforcement for concrete structures. Smart Materials and Structures, 2010, 19(2): 025011
18. Panda S K, Singh B N. Nonlinear finite element analysis of thermal post-buckling vibration of laminated composite shell panel embedded with SMA fibre. Aerospace Science and Technology, 2013, 29(1): 47–57
19. Rodrigue H, Wang W, Bhandari B, et al. SMA-based smart soft composite structure capable of multiple modes of actuation. Composites. Part B, Engineering, 2015, 82: 152–158
20. Daghash S M, Ozbulut O E. Characterization of superelastic shape memory alloy fiber-reinforced polymer composites under tensile cyclic loading. Materials & Design, 2016, 111: 504–512
21. Sofocleous K, Drakonakis V M, Ogin S L, et al. The influence of carbon nanotubes and shape memory alloy wires to controlled impact resistance of polymer composites. Journal of Composite Materials, 2017, 51(2): 273–285
22. El-Tahan M, Dawood M. Bond behavior of NiTiNb SMA wires embedded in CFRP composites. Polymer Composites, 2018, 39(10): 3780–3791
23. Mahmood Baitab D, Laila Abang Haji Abdul Majid D, Junita Abdullah E, et al. A review of techniques for embedding shape memory alloy (SMA) wires in smart woven composites. International Journal of Engineering and Technology, 2018, 7(4.13): 129–136
24. Quade D J, Jana S C, Morscher G N, et al. The effect of thin film adhesives on mode II interlaminar fracture toughness in carbon fiber composites with shape memory alloy inserts. Mechanics of Materials, 2019, 131: 22–32
25. Eslami-Farsani R, Khazaie M. Effect of shape memory alloy wires on high-velocity impact response of basalt fiber metal laminates. Journal of Reinforced Plastics and Composites, 2018, 37(5): 300–309
26. Eslami-Farsani R, Mohaseb Karimlou M R, Saeedi A, et al. Effect of shape memory alloy wires on the buckling behavior of fiber metal laminates. Fibers and Polymers, 2019, 20(8): 1690–1695

27. Pazhanivel K, Bhaskar G B, Elayaperumal A, et al. Influence of SMA reinforcement on the impact resistance of GFRP composite laminates under different temperatures. Bulletin of Materials Science, 2016, 39(3): 889–899
28. Pazhanivel K, Bhaskar G B, Elayaperumal A, et al. Influence of Ni–Ti shape memory alloy short fibers on the flexural response of glass fiber reinforced polymeric composites. SN Applied Sciences, 2019, 1(7): 789
29. Sun Z, Xu Y, Wang W. Experimentation of the bilinear elastic behavior of plain-woven GFRP composite with embedded SMA wires. Polymers, 2019, 11(3): 405
30. Wang J, Moumni Z, Zhang W, et al. A thermomechanically coupled finite deformation constitutive model for shape memory alloys based on Hencky strain. International Journal of Engineering Science, 2017, 117: 51–77
31. Nie Z. Advanced mesomechanical modeling of triaxially braided composites for dynamic impact analysis with failure. Dissertation for the Doctoral Degree. Akron: The University of Akron, 2014
32. Yang B, Lei H, Wang Z, et al. Effects of SMA filament surface nano SiO_2 modification on interface bonding strength of SMA/epoxy composites. Acta Materiae Compositae Sinica, 2015, 32(5): 1341–1348 (in Chinese)